Ground-state computation of Bose-Einstein condensates by an imaginary-time quantum lattice Boltzmann scheme

S. Palpacelli,[1] S. Succi,[2] and R. Spigler[1]
[1]*Dipartimento di Matematica, Università Roma Tre, Largo San Leonardo Murialdo 1, 00146, Roma, Italy*
[2]*Istituto Applicazioni del Calcolo, Viale Policlinico 137, 00161 Roma, Italy*
(Received 5 June 2007; revised manuscript received 3 September 2007; published 28 September 2007)

The multidimensional formulation of the quantum lattice Boltzmann (qLB) scheme is extended to the case of nonlinear quantum wave equations. More specifically, imaginary-time formulations of the qLB scheme are developed and applied to the numerical computation of the ground state of the Gross-Pitaevskii equation in one and two spatial dimensions. The calculation is validated through detailed comparison with other numerical methods, as well as with analytical results based on the Thomas-Fermi approximation. The linear scaling of the time-step size with the spatial mesh spacing, a distinctive feature of the present quantum kinetic approach, is also numerically demonstrated.

DOI: 10.1103/PhysRevE.76.036712 PACS number(s): 02.70.−c, 03.65.−w

I. INTRODUCTION

The staggering achievements in Bose-Einstein condensation [1,2] over the last decade are fueling an increasing demand of efficient and accurate computational schemes for the numerical solution of nonlinear quantum wave equations, most notably, the Gross-Pitaevskii equation describing zero-temperature Bose-Einstein condensates [3,4]. A large variety of numerical methods exists, which can be roughly split into two major categories: explicit and implicit. In the latter, the wave function at present time t and at a given spatial location x is computed solely in terms of its values in a local neighborhood of x at a previous time $t-\Delta t$, in full compliance with the principle of local causality. The resulting computational schemes are fast and simple, but suffer from severe time step limitations, due to the stability limits imposed by causality, typically a quadratic scaling of the time step with the mesh size, as a result of the diffusive nature of the kinetic energy operator (Laplacian). Such time-step limitations are usually circumvented by moving to implicit methods, whereby the state at x and t depends on all spatial locations at the previous time $t-\Delta t$, thereby violating the principle of local causality. The result is a "global" dynamics which can proceed at much larger steps without incurring any numerical instability. The price for such an accelerated dynamics is that each single time steps requires much more computations since all sites have to be processed simultaneously (matrix problem). In addition, the use of large time steps must be constantly weighted against accuracy requirements, if details of the dynamical evolution are to be correctly captured. Because of this, implicit methods are most suited to ground-state computations, in which dynamical details are basically irrelevant, the only focus being on the time-asymptotic properties, i.e., ground state. Obviously, one would like to achieve an optimal blend of these complementary properties, i.e., a numerical scheme featuring stable operation with a low computational cost per time step, yet progressing to steady state in relative large time steps. Recently, a class of methods offering such potential have been developed [5,6] in the form of so-called quantum lattice Boltzmann (qLB) schemes. Originally, qLB builds on a formal analogy between the Dirac equation and a Boltzmann equation for a complex distribution function [7,8]. It was then shown that the nonrelativistic Schrödinger equation follows from the complex Boltzmann equation under the same adiabatic assumptions (in imaginary time) which take the Boltzmann equation for classical molecules into the Navier-Stokes equations of continuum fluid mechanics. Based on this analogy, a quantum lattice Boltzmann scheme was formulated, in which the discrete speeds are identified with the four-spinor components of the Dirac's wave function. Very recently, multidimensional versions of qLB for the linear Schrödinger equation have been demonstrated too [9]. In this work, we take one step further, and extend the qLB methodology to the case of nonlinear quantum wave equations, most notably the Gross-Pitaevskii equation describing the dynamics of zero-temperature Bose-Einstein condensates. The nonlinear qLB is applied to the numerical computation of the ground state of the GPE in one and two dimensions, and its viability demonstrated through systematic comparison with numerical solutions obtained via standard implicit methods, as well as with analytical results based on the Thomas-Fermi approximation.

II. THE TIME-DEPENDENT GROSS-PITAEVSKII EQUATION

At zero temperature, the dynamics of a trapped Bose-Einstein condensates (BEC) is described by the time-dependent Gross-Pitaevskii equation (GPE). The GPE for a quantum wave function $\psi(\boldsymbol{r},t)$ with $\boldsymbol{r}=(x,y,z)^T \in \mathbb{R}^3$ reads

$$i\hbar \frac{\partial \psi(\boldsymbol{r},t)}{\partial t} = \left(-\frac{\hbar^2}{2m}\Delta_{\boldsymbol{r}} + V_{\text{ext}}(\boldsymbol{r}) + NU_0|\psi(\boldsymbol{r},t)|^2 \right)\psi(\boldsymbol{r},t), \tag{1}$$

where m is the atomic mass, $U_0=4\pi\hbar^2 a/m$ is the coupling strength, a is the scattering length, N is the number of particles in the condensate, and $V_{\text{ext}}(\boldsymbol{r})$ is the external trapping potential. Furthermore, the wave function $\psi(\boldsymbol{r},t)$ satisfies the normalization condition

$$\int_{\mathbb{R}^3} |\psi(\boldsymbol{r},t)|^2 d\boldsymbol{r} = 1.$$

Typically, the external potential is taken in the form of an harmonic trap

$$V_{\text{ext}}(x,y,z) = \frac{1}{2} m[\omega_x^2(x-x_0)^2 + \omega_y^2(y-y_0)^2 + \omega_z^2(z-z_0)^2].$$

The three-dimensional GPE can be reduced to two dimensions or even one dimension for two particular choices of the harmonic trap [10–13]. We briefly revisit this reduction procedure following [12].

Disk-shaped condensation.

$$\omega_x \approx \omega_y, \quad \omega_z \gg \omega_x.$$

The three-dimensional GPE of Eq. (1) can be reduced to a two-dimensional GPE by assuming that the time evolution does not affect the wave function along the z axis. Thus, one assumes that the wave function along z is always well described by the ground-state wave function $\phi_g(x,y,z)$:

$$\psi(x,y,z,t) = \psi_{xy}(x,y,t)\psi_z(z) \quad \text{with}$$

$$\psi_z(z) = \left(\int_{\mathbb{R}^2} |\phi_g(x,y,z)|^2 dxdy \right)^{1/2}.$$

By means of this assumption the GPE of Eq. (1) is reduced to a two-dimensional GPE for $\boldsymbol{r}=(x,y)^T$ of the same form of Eq. (1), where the coupling strength is now given by

$$\tilde{U}_0 = U_0 \int_{\mathbb{R}} \psi_z^4(z) dz.$$

Cigar-shaped condensation.

$$\omega_y \gg \omega_x, \quad \omega_z \gg \omega_x.$$

In this case, the three-dimensional GPE can be reduced to a one-dimensional GPE for $\boldsymbol{r}=x$. As in the previous case, one assumes that the wave function along y and z is always well described by the ground state $\phi_g(x,y,z)$

$$\psi(x,y,z,t) = \psi_x(x,t)\psi_{yz}(y,z) \quad \text{with}$$

$$\psi_{yz}(y,z) = \left(\int_{\mathbb{R}} |\phi_g(x,y,z)|^2 dx \right)^{1/2}.$$

The GPE of Eq. (1) is then reduced to a one dimensional GPE of the same form, where the coupling strength is given by

$$\tilde{U}_0 = U_0 \int_{\mathbb{R}^2} \psi_{yz}^4(y,z) dydz.$$

In the following we will consider the GPE in the following form:

$$i\hbar \frac{\partial \psi(\boldsymbol{r},t)}{\partial t} = \left(-\frac{\hbar^2}{2m}\Delta_{\boldsymbol{r}} + V_{\text{ext}}(\boldsymbol{r}) + NU_d|\psi(\boldsymbol{r},t)|^2 \right)\psi(\boldsymbol{r},t), \tag{2}$$

for $\boldsymbol{r} \in \mathbb{R}^d$ with $d=1,2,3$ and

$$U_d = \begin{cases} U_0 \displaystyle\int_{\mathbb{R}^2} \psi_{yz}^4 dydz, & d=1, \\ U_0 \displaystyle\int_{\mathbb{R}} \psi_z^4 dz, & d=2 \\ U_0, & d=3. \end{cases} \tag{3}$$

Furthermore, we require

$$\int_{\mathbb{R}^d} |\psi(\boldsymbol{r})|^2 d\boldsymbol{r} = 1.$$

However, in this work, we solve Eq. (2) in one and two dimensions using NU_d as a coupling parameter. In particular, we do not compute U_d from Eq. (3), we simply consider the value of $NU_d \equiv V_{nl}$ as a measure of the interaction strength. Moreover, we do not use the classical scaling usually applied to make the GPE dimensionless, but a qLB scaling (see Appendix for details) which transforms Eq. (1) into

$$i\frac{\partial \psi(\boldsymbol{r},t)}{\partial t} = \left(-\frac{1}{2\tilde{m}}\Delta_{\boldsymbol{r}} + V_{\text{ext}}(\boldsymbol{r}) + V_{nl}|\psi(\boldsymbol{r},t)|^2 \right)\psi(\boldsymbol{r},t), \tag{4}$$

where all quantities are expressed in lattice units and $\tilde{m} = \omega_c \Delta t$ [see Eq. (A9)]. Unless differently stated, in our numerical examples $V_{\text{ext}}(\boldsymbol{r})$ is a harmonic potential in one and two dimensions and is given by

$$V_{\text{ext}}(x) = \frac{1}{2}\tilde{m}\omega_x^2(x-x_0)^2, \quad d=1, \tag{5}$$

$$V_{\text{ext}}(x,y) = \frac{1}{2}\tilde{m}[\omega_x^2(x-x_0)^2 + \omega_y^2(y-y_0)^2], \quad d=2, \tag{6}$$

where again lattice units are used.

III. THE GROUND-STATE SOLUTION OF THE GPE

Following Refs. [14,15], we derive the nonlinear eigenvalue problem from which one can compute the ground-state solution of the GPE of Eq. (2). In order to find a stationary solution of Eq. (2), we set

$$\psi(\boldsymbol{r},t) = e^{-i\mu t}\phi(\boldsymbol{r}), \tag{7}$$

where μ is the chemical potential of the condensate and $\phi(\boldsymbol{r})$ is a real-valued function independent of time. Inserting Eqs. (7) into (2), we find the following equation for $\phi(\boldsymbol{r})$:

$$\mu\phi(\boldsymbol{r}) = \left(-\frac{\hbar}{2m}\Delta_{\boldsymbol{r}} + \frac{V_{\text{ext}}(\boldsymbol{r})}{\hbar} + \frac{NU_d}{\hbar}|\phi(\boldsymbol{r})|^2 \right)\phi(\boldsymbol{r}), \tag{8}$$

with the normalization condition

$$\int_{\mathbb{R}^d} |\phi(\boldsymbol{r})|^2 d\boldsymbol{r} = 1. \tag{9}$$

This is a nonlinear eigenvalue problem under a constraint and any eigenvalue μ can be computed from its corresponding eigenfunction ϕ. In particular, multiplying Eq. (7) by $\phi(\boldsymbol{r})$ and integrating we obtain

$$\mu = \int_{\mathbb{R}^d} \left(-\frac{\hbar}{2m}[\Delta_{\boldsymbol{r}}\phi(\boldsymbol{r})]\phi(\boldsymbol{r}) + \frac{V_{\text{ext}}(\boldsymbol{r})}{\hbar}|\phi(\boldsymbol{r})|^2 + \frac{NU_d}{\hbar}|\phi(\boldsymbol{r})|^4 \right) d\boldsymbol{r}.$$

Thus, integrating by parts the first term of the right-hand side, we have

$$\mu = \int_{\mathbb{R}^d} \left(\frac{\hbar}{2m}|\nabla_{\boldsymbol{r}}\phi(\boldsymbol{r})|^2 + \frac{V_{\text{ext}}(\boldsymbol{r})}{\hbar}|\phi(\boldsymbol{r})|^2 + \frac{NU_d}{\hbar}|\phi(\boldsymbol{r})|^4 \right) d\boldsymbol{r}. \tag{10}$$

The ground-state solution of the Bose-Einstein condensate $\phi_g(\boldsymbol{r})$ is a real-valued function which can be found by minimizing Eq. (10) under the constraint of Eq. (9). Typically, this minimizer is found by applying to Eq. (2) a transformation, known as Wick rotation, which consists on "rotating" the time axis on the complex plane so that time becomes purely imaginary [16–19]. With this rotation of the time axis, the GPE of Eq. (2) becomes a diffusion equation with an absorption or emission term given by the potential.

Wick rotation consists of introducing an imaginary variable τ which is related to the time t by the relation $t=-i\tau$. Applying this transformation to Eq. (2), we have

$$\hbar\frac{\partial\psi(\boldsymbol{r},\tau)}{\partial\tau} = \left(\frac{\hbar^2}{2m}\Delta_{\boldsymbol{r}} - V_{\text{ext}}(\boldsymbol{r}) - NU_d|\psi(\boldsymbol{r},\tau)|^2 \right)\psi(\boldsymbol{r},\tau). \tag{11}$$

Finally, our problem is to solve Eq. (11) under the constraint

$$\int_{\mathbb{R}^d} |\psi(\boldsymbol{r},t)|^2 d\boldsymbol{r} = 1. \tag{12}$$

Applying the qLB scaling (see Appendix) to Eq. (11) and hence expressing all quantities in lattice units, Eq. (11) becomes

$$\frac{\partial\psi(\boldsymbol{r},\tau)}{\partial\tau} = \left(\frac{1}{2\tilde{m}}\Delta_{\boldsymbol{r}} - V_{\text{ext}}(\boldsymbol{r}) - V_{nl}|\psi(\boldsymbol{r},\tau)|^2 \right)\psi(\boldsymbol{r},\tau), \tag{13}$$

where $\tilde{m}=\omega_c\Delta t$ [see Eq. (A9)] and $V_{\text{ext}}(\boldsymbol{r})$ is given by Eqs. (5) and (6).

IV. THE IMAGINARY-TIME QUANTUM LATTICE BOLTZMANN MODEL

The model we propose is obtained by applying the Wick rotation to the quantum lattice Boltzmann model (qLB) [7–9]. We recall that the qLB is based on a formal analogy between the Dirac quadrispinor $\psi=(u_1,u_2,d_1,d_2)^T$ and the discrete distribution functions of the lattice Boltzmann equation [7]. By using an operator splitting approach, the model can be easily extended to two and three dimensions [7,9].

Being based on a first-order, relativistic formulation, at variance with most explicit schemes for nonrelativistic quantum wave equations, the qLB method offers unconditional stability with the size of the time step and mesh size. However, its accuracy is subject to the condition $\omega_c\Delta t=\Delta x/\lambda_B \leqslant 1$, $\lambda_B=c/\omega_c$ being the De Broglie wavelength of the particle and $\omega_c=mc^2/\hbar$ being the Compton frequency. Since the time step scales linearly with the mesh spacing (a result of the relativistic formulation), qLB can be taken down to very refined grids without suffering the time-step collapse typical of nonrelativistic Courant-Friedrichs-Lewy stability conditions $\Delta t < \frac{2m}{\hbar}\Delta x^2$. On the other hand, violations of adiabaticity in the region $\omega_c\Delta t \ll 1$ must be carefully watched in order to preserve the validity of qLB in the nonrelativistic regime.

Here, we show that, by applying the Wick rotation to the qLB model, we obtain a scheme for the computation of the ground-state solution for the GPE. For the sake of simplicity, we first describe the scheme in one and two dimensions for the free-particle case ($V_{\text{ext}}=0$ and $V_{nl}=0$), and subsequently discuss how to include interactions in the model.

A. Imaginary-time qLB in one dimension

Consider the Dirac equation in one dimension. Using the Majorana representation [20], and projecting upon chiral eigenstates, the Dirac equation reads

$$\partial_t u_{1,2} + c\partial_x u_{1,2} = \omega_c d_{2,1},$$

$$\partial_t d_{1,2} - c\partial_x d_{1,2} = -\omega_c u_{2,1}, \tag{14}$$

where $\omega_c=mc^2/\hbar$ is the Compton frequency.

We introduce the imaginary variable $\tau=it$ and write Eq. (14) in terms of τ:

$$\partial_\tau u_{1,2} - ic\partial_x u_{1,2} = -i\omega_c d_{2,1},$$

$$\partial_\tau d_{1,2} + ic\partial_x d_{1,2} = i\omega_c u_{2,1}. \tag{15}$$

Let $\Delta\tau=i\Delta t$ be the time discretization step (note that $\Delta\tau$ is a purely imaginary number) and $\Delta x=-ic\Delta\tau$ the spatial discretization step. Integrating Eq. (15) between τ and $\tau+\Delta\tau$ and approximating the right-hand side integral by

$$\int_\tau^{\tau+\Delta\tau} d_{2,1}(x,\tau)d\tau \sim \frac{1}{2}\Delta\tau[d_{2,1}(x-\Delta x,\tau+\Delta\tau)+d_{2,1}(x,\tau)],$$

$$\int_\tau^{\tau+\Delta\tau} u_{2,1}(x,\tau)d\tau \sim \frac{1}{2}\Delta\tau[u_{2,1}(x+\Delta x,\tau+\Delta\tau)+u_{2,1}(x,\tau)],$$

we obtain

$$u_{1,2}(x+\Delta x,\tau+\Delta\tau) - u_{1,2}(x,\tau) = -i\frac{\omega_c}{2}[d_{2,1}(x-\Delta x,\tau+\Delta\tau)+d_{2,1}(x,\tau)]\Delta\tau,$$

$$d_{1,2}(x-\Delta x,\tau+\Delta\tau)-d_{1,2}(x,\tau)$$

$$=i\frac{\omega_c}{2}[u_{2,1}(x+\Delta x,\tau+\Delta\tau)+u_{2,1}(x,\tau)]\Delta\tau. \quad (16)$$

By defining

$$\omega_c\Delta t\equiv\tilde{m},$$

assuming $\Delta x=-ic\Delta\tau=1$ and using atomic units ($c=1$, $\hbar=1$), we obtain

$$\hat{u}-u=-i\tilde{m}\left(\frac{\hat{d}+d}{2}\right),$$

$$\hat{d}-d=i\tilde{m}\left(\frac{\hat{u}+u}{2}\right), \quad (17)$$

where $\hat{u}=u(x+1,\tau+i)$, $\hat{d}=d(x-1,\tau+i)$, $u=u(x,\tau)$, and $d=d(x,\tau)$. Note that, for $c=1$, $\tilde{m}=m$. However, as we shall clarify in Appendix, in order to simulate BEC physics, one needs to assume c much smaller than the physical light speed.

The system of Eq. (17) can be algebraically solved for $\hat{u}$ and $\hat{d}$ and yields the imaginary-time qLB model

$$\hat{u}=au-bd,$$

$$\hat{d}=ad+bu, \quad (18)$$

where

$$a=\frac{1+\tilde{m}^2/4}{1-\tilde{m}^2/4},\quad b=\frac{i\tilde{m}}{1-\tilde{m}^2/4}. \quad (19)$$

Note that $|a|^2+|b|^2\neq 1$, hence the collision matrix is not unitary. This implies that the model does not verify the normalization condition, as it happens for the real-time version of the scheme This is usual for models which compute the ground state solution by solving dynamic equations in fictitious time, such as Eq. (11). Hence, the normalization condition of Eq. (12) must be imposed at each time step by directly normalizing the wave function [14,15,18]. In the qLB model, the normalization step is performed by defining

$$\|\psi(x,\tau)\|^2=|u_1(x,\tau)|^2+|u_2(x,\tau)|^2+|d_1(x,\tau)|^2+|d_2(x,\tau)|^2,$$

and then dividing $u_{1,2}$ and $d_{1,2}$ by $\|\psi(x,\tau)\|$.

In analogy with the real-time qLB, we define the wave functions

$$\phi^{\pm}_{1,2}=\frac{1}{\sqrt{2}}e^{\tilde{m}\tau}(u_{1,2}\pm id_{2,1}). \quad (20)$$

Since $u_{1,2}$ and $d_{1,2}$ fulfill Eq. (15), $\phi^{\pm}_{1,2}$ satisfy the following equations:

$$\partial_\tau\phi^{+}_{1,2}-i\partial_x\phi^{-}_{1,2}=0, \quad (21)$$

$$\partial_\tau\phi^{-}_{1,2}-i\partial_x\phi^{+}_{1,2}=2\tilde{m}\phi^{-}_{1,2}. \quad (22)$$

By taking the x derivative of Eq. (21), multiplying Eq. (22) by i, and deriving it with respect to τ and then subtracting the resulting equations, we obtain the following equation for $\phi^{-}_{1,2}$:

$$\partial_\tau\phi^{-}_{1,2}=\frac{1}{2\tilde{m}}\partial_x^2\phi^{-}_{1,2}+\frac{1}{2\tilde{m}}\partial_\tau^2\phi^{-}_{1,2}. \quad (23)$$

The second order time derivative term drives an instability which tends to amplify $\phi^{-}_{1,2}$ while preserving its spatial profile. However, the normalization step tames the effect of this term. We will clarify this point in the following, through the analysis of the dispersion relation of the governing equation for $\phi^{-}_{1,2}$ when a potential is switched on (see Sec. VI). Here, we just observe that for the free-particle case ($V_{\text{ext}}=0$ and $V_{nl}=0$), $\phi^{-}_{1,2}$ obey a diffusion equation with the correct diffusion coefficient [see Eq. (13)].

The wave functions $\phi^{-}_{1,2}$ are the ones whose dynamics tends to the ground-state solution of the GPE, while the wave functions $\phi^{+}_{1,2}$ are fast ("ghost") variables, which are initialized at zero and remain negligible all along the simulation, as compared to $\phi^{-}_{1,2}$. When a potential is included, the analysis of the governing equation for $\phi^{-}_{1,2}$ is not as simple as in the free-particle case. Hence, in the following subsection, we show how to include the potential effect in the model, while in Sec. VI we discuss in a more detail the equation satisfied by $\phi^{-}_{1,2}$ in the interacting case.

B. Adding a potential to the imaginary-time qLB

As we mentioned above, the wave function ϕ^{-} tends to the ground-state solution, hence, in the imaginary-time qLB, the total potential of the GPE of Eq. (2) in one spatial dimension is defined as follows:

$$V(x,\tau)=V_{\text{ext}}(x)+V_{nl}|\phi^{-}|^2. \quad (24)$$

To include the effect of this potential into the model, we consider the Dirac equation with a potential and apply to this equation the Wick rotation. This yields

$$\partial_\tau u_{1,2}-ic\partial_x u_{1,2}=-i\omega_c d_{2,1}+gu_{1,2},$$

$$\partial_\tau d_{1,2}+ic\partial_x d_{1,2}=i\omega_c u_{2,1}+gd_{1,2}, \quad (25)$$

where $g=qV/\hbar$ and q is the particle electric charge.

Applying to Eqs. (25) the same discretization already described for the free particle case and assuming $c=1$, $\hbar=1$, and $q=-1$, we obtain the following scheme:

$$\hat{u}=a_g u-b_g d,$$

$$\hat{d}=a_g d+b_g u, \quad (26)$$

where

$$a_g=\frac{(1-g/2)(1+g/2)+\tilde{m}^2/4}{(1-g/2)^2-\tilde{m}^2/4},\quad b_g=\frac{i\tilde{m}}{(1-g/2)^2-\tilde{m}^2/4}, \quad (27)$$

and $\hat{u}=u(x+1,\tau+i)$, $\hat{d}=d(x-1,\tau+i)$, $u=u(x,\tau)$, and $d=d(x,\tau)$, where we have also assumed $\Delta x=-ic\Delta\tau=1$ for simplicity. Note that g is evaluated at time τ, i.e., there is no

iteration over the nonlinearity. For real-time computations this might hamper norm conservation, but in the case of the present ground-state computations this is not an issue because the norm is not conserved in time due to the potential interactions.

V. EXTENSION TO TWO SPATIAL DIMENSIONS

As for the one-dimensional case, we describe how to extend the model to two spatial dimensions (extension to three dimensions is a straightforward generalization of this procedure) in the absence of a potential. The inclusion of a potential is completely analogous to the one-dimensional case.

The extension to higher dimensions is based on an operator splitting approach and follows the strategy already used to extend the real-time qLB model to the two- and three-dimensional case [7,9].

Let us consider the two-dimensional Dirac equation in Majorana form [20], so that all spin matrices have real coefficients. Furthermore, we apply to the equation a transformation in order to diagonalize the matrix of the $\partial_x \psi$ term. With these assumptions, the equation reads

$$[\partial_t + cA_x\partial_x + cA_y\partial_y]\psi(x,y,t) = \omega_c C\psi(x,y,t), \tag{28}$$

where

$$A_x = \begin{pmatrix} 1 & 0 & 0 & 0 \\ 0 & 1 & 0 & 0 \\ 0 & 0 & -1 & 0 \\ 0 & 0 & 0 & -1 \end{pmatrix},$$

$$A_y = \begin{pmatrix} 0 & 0 & -1 & 0 \\ 0 & 0 & 0 & -1 \\ -1 & 0 & 0 & 0 \\ 0 & -1 & 0 & 0 \end{pmatrix}, \quad C = \begin{pmatrix} 0 & 0 & 0 & 1 \\ 0 & 0 & 1 & 0 \\ 0 & -1 & 0 & 0 \\ -1 & 0 & 0 & 0 \end{pmatrix}.$$

Applying to Eq. (28) the Wick rotation, we obtain

$$[\partial_\tau + c\tilde{A}_x\partial_x + c\tilde{A}_y\partial_y]\psi(x,y,\tau) = \omega_c \tilde{C}\psi(x,y,\tau), \tag{29}$$

where

$$\tilde{A}_x = \begin{pmatrix} -i & 0 & 0 & 0 \\ 0 & -i & 0 & 0 \\ 0 & 0 & i & 0 \\ 0 & 0 & 0 & i \end{pmatrix} \quad \tilde{A}_y = \begin{pmatrix} 0 & 0 & i & 0 \\ 0 & 0 & 0 & i \\ i & 0 & 0 & 0 \\ 0 & i & 0 & 0 \end{pmatrix}$$

$$\tilde{C} = \begin{pmatrix} 0 & 0 & 0 & -i \\ 0 & 0 & -i & 0 \\ 0 & i & 0 & 0 \\ i & 0 & 0 & 0 \end{pmatrix}.$$

To solve Eq. (29) we use the same sequential splitting technique already introduced for the real-time qLB [9]. In particular, in the interval $[(n-1)\Delta\tau, n\Delta\tau]$, we consider the sequence of the two problems

$$\begin{cases} \partial_\tau \psi_1^n + c\tilde{A}_x\partial_x\psi_1^n = \dfrac{\omega_c}{2}\tilde{C}\psi_1^n, \\ \psi_1^n[(n-1)\Delta\tau] = \psi_2^{n-1}[(n-1)\Delta\tau] \end{cases} \tag{30}$$

and

$$\begin{cases} \partial_\tau \psi_2^n + c\tilde{A}_y\partial_y\psi_2^n = \dfrac{\omega_c}{2}\tilde{C}\psi_2^n, \\ \psi_2^n[(n-1)\Delta\tau] = \psi_1^n(n\Delta\tau), \end{cases} \tag{31}$$

for $n=1,2,\ldots$. To start the procedure we set $\psi_2^0(0)=\psi_0$ and, at time $n\Delta\tau$, the approximated solution is given by $\psi_2^n(x,y,n\Delta\tau)$.

After this splitting, the two-dimensional problem of Eq. (29) is transformed into a sequence of two one-dimensional problems. In particular, problem of Eq. (30) is analogous to the system of Eq. (15), with the only difference being a factor $1/2$ in front of matrix $\tilde{C}$. Hence, to solve Eq. (30), the scheme of Eq. (18) [or scheme of Eq. (26) if the potential is switched on] is used, where a and b (or a_g and b_g) are slightly changed due to the factor $1/2$. In particular, a and b are defined as

$$a = \frac{1+\bar{m}^2/4}{1-\bar{m}^2/4}, \quad b = \frac{i\bar{m}}{1-\bar{m}^2/4}, \tag{32}$$

while a_g and b_g are given by

$$a_g = \frac{(1-\bar{g}/2)(1+\bar{g}/2)+\bar{m}^2/4}{(1-\bar{g}/2)^2-\bar{m}^2/4}, \quad b_g = \frac{i\bar{m}}{(1-\bar{g}/2)^2-\bar{m}^2/4}, \tag{33}$$

with $\bar{m}=\tilde{m}/2$ and $\bar{g}=g/2$.

In order to solve problem of Eq. (31) by means of a qLB scheme, the equation must be transformed into an equivalent one where matrix $\tilde{A}_y$ is diagonal. In practice, we apply to $\tilde{A}_y$, $\tilde{C}$, and ψ the transformation Y:

$$Y = \frac{1}{\sqrt{2}}\begin{pmatrix} -1 & 0 & 0 & 1 \\ 0 & -1 & 1 & 0 \\ 1 & 0 & 0 & 1 \\ 0 & 1 & 1 & 0 \end{pmatrix}.$$

After this transformation, writing explicitly Eq. (31), we obtain

$$\partial_\tau u_{1,2}^y - ic\partial_y u_{1,2}^y = i\frac{\omega_c}{2}d_{1,2},$$

$$\partial_\tau d_{1,2}^y + ic\partial_y d_{1,2}^y = -i\frac{\omega_c}{2}u_{1,2}, \tag{34}$$

where we indicate with $u_{1,2}^y$ and $d_{1,2}^y$ the components of the transformed quadrispinor $\psi^y = Y\psi$.

From Eq. (34), using the same discretization scheme already described in the one-dimensional case and assuming $\Delta y = \Delta x = -ic\Delta\tau = 1$, $\hbar = 1$ and $c=1$, we obtain

$$\hat{u}_{1,2}^y = au_{1,2}^y + bd_{1,2}^y,$$

$$\hat{d}^y_{1,2} = a d^y_{1,2} - b u^y_{1,2},$$

with a and b as in Eq. (32) [or as in Eq. (33) if we include the potential]. Finally, we return to the original wave function via the inverse transformation $\psi = Y^{-1}\psi^y$.

As in one dimension, we define the wave functions $\phi^{\pm}_{1,2}$

$$\phi^{\pm}_{1,2} = \frac{1}{\sqrt{2}} e^{\tilde{m}\tau}(u_{1,2} \pm i d_{2,1}).$$

Since $u_{1,2}$ and $d_{1,2}$ fulfill Eq. (29), we have

$$\partial_\tau \phi^+_1 - i\partial_x \phi^-_1 - \partial_y \phi^-_2 = 0, \tag{35}$$

$$\partial_\tau \phi^+_2 - i\partial_x \phi^-_2 - \partial_y \phi^-_1 = 0 \tag{36}$$

and

$$\partial_\tau \phi^-_1 - i\partial_x \phi^+_1 + \partial_y \phi^+_2 = 2\tilde{m}\phi^-_1, \tag{37}$$

$$\partial_\tau \phi^-_2 - i\partial_x \phi^+_2 + \partial_y \phi^+_1 = 2\tilde{m}\phi^-_2. \tag{38}$$

By deriving Eq. (35) with respect to x, multiplying Eq. (36) by i and deriving it with respect to y, multiplying Eq. (37) by $-i$ and deriving it with respect to τ and finally summing up the resulting equations, we obtain

$$\partial_\tau \phi^-_1 = \frac{1}{2\tilde{m}}(\partial^2_x \phi^-_1 + \partial^2_y \phi^-_1) + \frac{1}{2\tilde{m}}\partial^2_\tau \phi^-_1.$$

Similarly, multiplying Eq. (35) by i and deriving it with respect to y, deriving Eq. (36) with respect to x, multiplying Eq. (38) by $-i$ and deriving it with respect to τ and finally summing up the resulting equations, we obtain

$$\partial_\tau \phi^-_2 = \frac{1}{2\tilde{m}}(\partial^2_x \phi^-_2 + \partial^2_y \phi^-_2) + \frac{1}{2\tilde{m}}\partial^2_\tau \phi^-_2.$$

In conclusion, we obtain in two dimensions the same result we have derived in one dimension [see Eq. (23)]. The second order time derivative term represents once again an instability which is kept under control by the normalization step. The inclusion of the potential yields an equation for $\phi^-_{1,2}$, whose interpretation requires a more systematic analysis. To this purpose, we shall inspect the dispersion relation in order to verify that the model is solving the correct equation (see Sec. VI).

VI. DISPERSION RELATION FOR THE EQUATION GOVERNING ϕ^-

In this section, we derive the equation satisfied by $\phi^-_{1,2}$ and we analyze it by computing its dispersion relation. We will perform this computation only in one dimension, the two-dimensional generalization is, however, straightforward. In the following the indices 1, 2 on $\phi^-_{1,2}$ shall be dropped because the dynamics of the two wave functions is exactly the same. In order to check that ϕ^- has a correct asymptotic behavior, we derive the dispersion relation of the equation we intend to be solved by ϕ^-. Hence, suppose that ϕ^- is a solution of the imaginary-time GPE of Eq. (13) (using qLB scaling). Let us rewrite Eq. (13) as

$$\partial_\tau \phi^- = \frac{1}{2\tilde{m}}\partial^2_x \phi^- - V\phi^-, \tag{39}$$

where

$$V(x,\tau) = \frac{1}{2\tilde{m}}\omega^2_x x^2 + V_{nl}|\phi^-|^2. \tag{40}$$

Note that the computation of the dispersion relation is not a rigorous procedure in this case because V is space and time dependent. However, this analysis can be useful in the limit where the potential does not change in time (because a stationary solution is reached) and is changing very slowly in space (at least in the region where $\phi^- \neq 0$). Hence, locally, we can think of V as of a constant and compute the dispersion relation in the "WKB" spirit. Assuming $\phi^- \sim e^{i(kx-\omega\tau)}$ and inserting this into Eq. (39), we obtain

$$\omega = -i\left(\frac{k^2}{2\tilde{m}} + V\right). \tag{41}$$

This is the "correct" dispersion relation we will refer to.

However, ϕ^- is not solving exactly Eq. (39). To derive the governing equation for ϕ^- we need to start from the Dirac equation given in Eq. (25) fulfilled by $u_{1,2}$ and $d_{1,2}$. Using atomic units ($c=1$, $\hbar=1$, $q=-1$) and dropping indices, we have

$$\partial_\tau u - i\partial_x u = -i\tilde{m}d - Vu,$$

$$\partial_\tau d + i\partial_x d = i\tilde{m}u - Vd,$$

where V is defined as in Eq. (40).

From u and d we define $\phi^{\pm} = \exp(\tilde{m}\tau)(u \pm id)/\sqrt{2}$ and one can easily show that for $\phi^{\pm}$ the following equations yield

$$\partial_\tau \phi^+ - i\partial_x \phi^- = -V\phi^+, \tag{42}$$

$$\partial_\tau \phi^- - i\partial_x \phi^+ = 2\tilde{m}\phi^- - V\phi^-. \tag{43}$$

On the assumption $V \sim$ const, we derive Eq. (42) with respect to x and Eq. (43) with respect to τ. We then multiply Eq. (43) by i and subtract the resulting equations, to finally obtain

$$\partial_\tau \phi^- = \frac{1}{2\tilde{m}}\partial^2_x \phi^- + \frac{1}{2\tilde{m}}\partial^2_\tau \phi^- + \frac{V}{2\tilde{m}}(\partial_\tau \phi^- + i\partial_x \phi^+). \tag{44}$$

From Eq. (43), we have

$$\partial_\tau \phi^- + i\partial_x \phi^+ = 2\partial_\tau \phi^- - 2\tilde{m}\phi^- + V\phi^- \tag{45}$$

and inserting Eq. (45) into Eq. (44) we obtain the governing equation for ϕ^-:

$$\partial_\tau \phi^- = \frac{1}{2\tilde{m}}\partial^2_x \phi^- - V\phi^- + \frac{1}{2\tilde{m}}(\partial^2_\tau \phi^- + 2V\partial_\tau \phi^- + V^2\phi^-). \tag{46}$$

Assuming $\phi^- \sim e^{i(kx-\omega\tau)}$ and inserting this into Eq. (46), we obtain

$$\omega^2 - 2i\omega(\tilde{m} - V) + k^2 + 2\tilde{m}V - V^2 = 0. \tag{47}$$

Solving Eq. (47), we obtain

TABLE I. Ground-state chemical potential μ for qLB, CN, and BEFD models. Numerical results are also compared with the Thomas-Fermi chemical potential [see Eq. (52)]. The results are computed for different values of V_{nl}, the other parameters are set as $\omega_x=1/128$, $\tilde{m}=1/8$, $\Delta_0=16$, $nx=1024$.

V_{nl}	μ qLB	μ CN	μ BEFD	μ TF
0	0.003906	0.003906	0.003906	
1	0.013678	0.013740	0.013740	0.012898
5	0.037978	0.038078	0.038071	0.037714
10	0.060007	0.060112	0.060112	0.059868
20	0.095084	0.095201	0.095201	0.095034
30	0.124540	0.124663	0.124663	0.124530
40	0.150843	0.150971	0.150971	0.150858
50	0.175024	0.175154	0.175154	0.175055
60	0.197637	0.197769	0.197769	0.197680
70	0.219023	0.219157	0.219157	0.219075
80	0.239412	0.239548	0.239548	0.239472

$$\omega_{\pm} = i(\tilde{m} - V) \pm i\sqrt{k^2 + \tilde{m}^2}.$$

Hence, for small values of k, we obtain

$$\omega_+ \approx -i\left(V - \frac{k^2}{2\tilde{m}} - 2\tilde{m}\right), \quad \omega_- \approx -i\left(\frac{k^2}{2\tilde{m}} + V\right).$$

In conclusion, ϕ^- is composed by two modes, ω_- is the correct stable mode we would expect according to Eq. (41), while ω_+ is a second mode, whose effect consists of a uniform amplification of ϕ^- and is dominated by $2\tilde{m}$ at long wavelengths $\frac{k^2}{2\tilde{m}} \ll V$. As previously discussed, the normalization step compensates this effect. In the sequel, we shall validate qLB for ground-state computations by comparing it against well-established methods such as Crank-Nicholson time marching and backward Euler finite difference scheme.

VII. A COMPARISON WITH THE CRANK-NICHOLSON AND BACKWARD EULER FINITE DIFFERENCE SCHEMES

Let us rewrite Eq. (13) for a real-valued function $\phi(\boldsymbol{r},\tau)$ (since the ground-state wave function is real valued):

$$\partial_\tau \phi(\boldsymbol{r},\tau) = \left(\frac{1}{2\tilde{m}}\Delta_{\boldsymbol{r}} - V_{\text{ext}}(\boldsymbol{r}) - V_{nl}|\phi(\boldsymbol{r},\tau)|^2\right)\phi(\boldsymbol{r},\tau), \quad (48)$$

with the normalization condition

$$\int_{\mathbb{R}^d} |\phi(\boldsymbol{r},\tau)|^2 d\boldsymbol{r} = 1. \quad (49)$$

Here we use the same scaling imposed by the qLB model (see Appendix for details). The external potential is given by Eqs. (5) and (6) in one and two dimensions, respectively.

In order to make a comparison and validate our results, Eq. (48) is solved by using the classical Crank-Nicholson (CN) and backward Euler finite difference (BEFD) schemes in the same computational domain and with the same set of parameters of the qLB. We note that to guarantee that $\phi(\boldsymbol{r},\tau)$ fulfills condition of Eq. (49) a normalization step is needed also for CN and BEFD schemes [14].

TABLE II. Maximum value reached by the ground-state profile $\phi_g(x_0)$ for qLB, CN, and BEFD models. The results are computed for different values of V_{nl}, the other parameters are set as $\omega_x=1/128$, $\tilde{m}=1/8$, $\Delta_0=16$, $nx=1024$.

V_{nl}	$\phi_g(z_0)$ qLB	$\phi_g(z_0)$ CN	$\phi_g(z_0)$ BEFD
0	0.1316	0.1327	0.1328
1	0.1105	0.1109	0.1109
5	0.0867	0.0868	0.0867
10	0.0773	0.0774	0.0774
20	0.0689	0.0689	0.0689
30	0.0644	0.0644	0.0644
40	0.0614	0.0614	0.0614
50	0.0591	0.0592	0.0592
60	0.0574	0.0574	0.0574
70	0.0559	0.0559	0.0559
80	0.0547	0.0547	0.0547

A. One-dimensional CN and BEFD schemes

Let us consider a computational domain $[x_{\min}, x_{\max}]$ subdivided into N subintervals of width $h=(x_{\max}-x_{\min})/N$. Furthermore, let k be the time step, x_i the nodal points and τ_n the discrete instants of time

$$x_i = x_{\min} + ih, \quad \tau_n = nk, \quad i = 0, \ldots, N, \quad n = 0,1,2, \ldots .$$

We indicate with ϕ_i^n the numerical approximation of $\phi(x_i,\tau_n)$ and with $\tilde{\phi}_i^n$ the non-normalized ϕ_i^n. With this notation, the CN scheme reads

$$\frac{\tilde{\phi}_i^{n+1} - \phi_i^n}{k} = \frac{1}{4\tilde{m}h^2}(\tilde{\phi}_{i+1}^{n+1} - 2\tilde{\phi}_i^{n+1} + \tilde{\phi}_{i-1}^{n+1} + \phi_{i+1}^n - 2\phi_i^n + \phi_{i-1}^n) - \frac{V_{\text{ext}}(x_i)}{2}(\tilde{\phi}_i^{n+1} + \phi_i^n) - \frac{V_{nl}}{2}|\phi_i^n|^2(\tilde{\phi}_i^{n+1} + \phi_i^n),$$

while the BEFD scheme is given by

$$\frac{\tilde{\phi}_i^{n+1} - \phi_i^n}{k} = \frac{1}{2\tilde{m}h^2}(\tilde{\phi}_{i+1}^{n+1} - 2\tilde{\phi}_i^{n+1} + \tilde{\phi}_{i-1}^{n+1}) - V_{\text{ext}}(x_i)\tilde{\phi}_i^{n+1} - V_{nl}|\phi_i^n|^2\tilde{\phi}_i^{n+1},$$

for $i=1,\ldots,N-1$ and $n=0,1,2,\ldots$.

Dirichlet boundary conditions are imposed for both schemes

$$\tilde{\phi}_0^{n+1} = \tilde{\phi}_N^{n+1} = 0,$$

and the normalization step is performed as follows:

$$\phi_i^{n+1} = \frac{\tilde{\phi}_i^{n+1}}{\|\tilde{\phi}^{n+1}\|},$$

for $i=0,\ldots,N$ and $n=0,1,2,\ldots$.

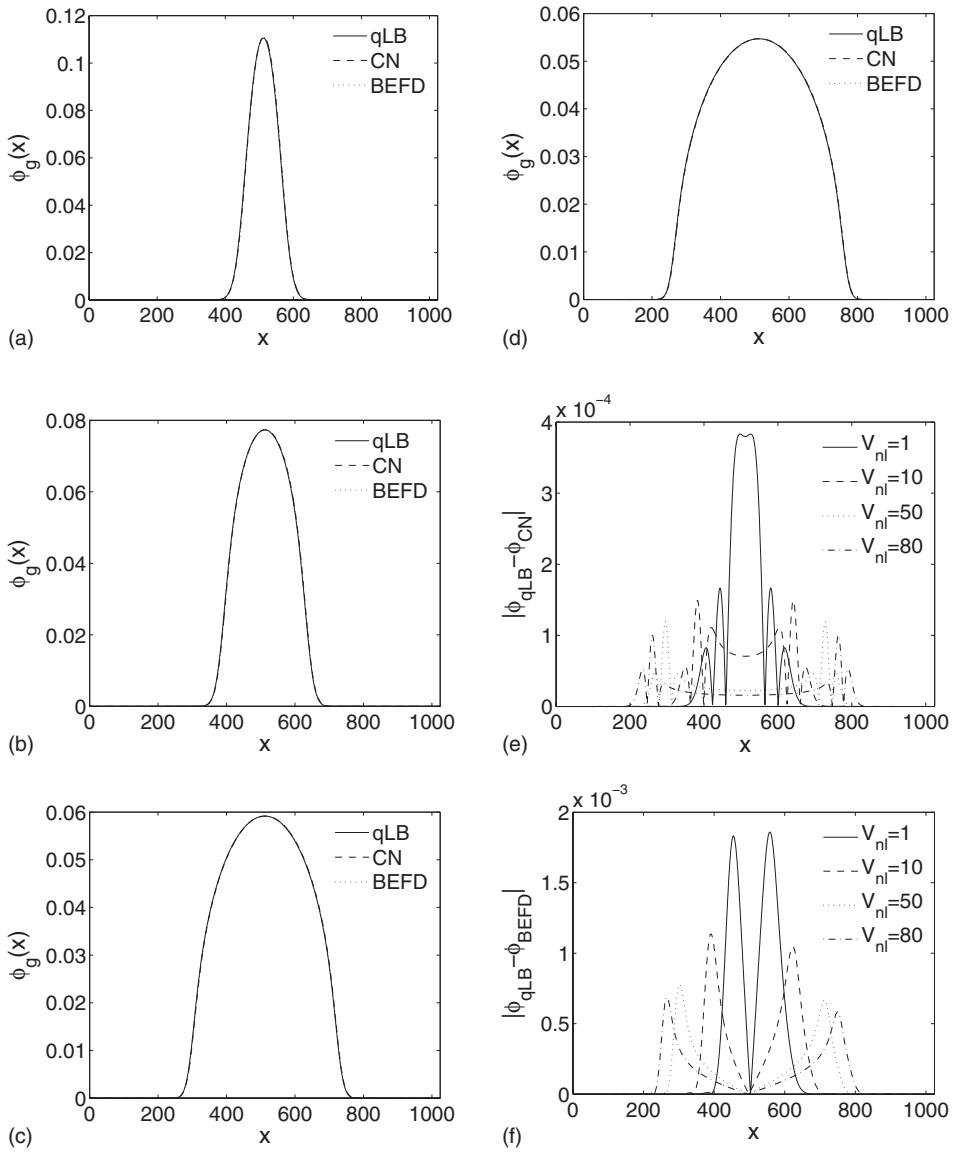

FIG. 1. Ground-state profile $\phi_g(x)$ for different values of V_{nl}. Simulation parameters are set as $\tilde{m}=1/8$, $\Delta_0=16$, $\omega_x=1/128$, $nx=1024$. (a) $V_{nl}=1$, (b) $V_{nl}=10$, (c) $V_{nl}=50$, (d) $V_{nl}=80$. Solid lines: qLB model; dashed lines: CN model; dotted lines: BEFD model. The deviations of qLB from CN and BEFD are not visible on this scale, hence in (e) and (f) the differences $|(\phi_g)_{\mathrm{qLB}}-(\phi_g)_{\mathrm{CN}}|$ and $|(\phi_g)_{\mathrm{qLB}}-(\phi_g)_{\mathrm{BEFD}}|$ computed at the qLB nodal points are plotted. Space is expressed in lattice units.

B. Two-dimensional CN and BEFD schemes

Let we consider a squared computational domain $[x_{\min},x_{\max}]\times[y_{\min},y_{\max}]\equiv[l_{\min},l_{\max}]\times[l_{\min},l_{\max}]$ and let we assume, for the sake of simplicity, $h_x=h_y\equiv h$. Hence, we subdivide $[l_{\min},l_{\max}]$ into $N_x=N_y\equiv N$ subintervals of width h. Furthermore, let be k the time step. We indicate with (x_i,y_j) the nodal points of the lattice and with τ_n the discrete instants of time:

$$x_i = l_{\min} + ih, \quad y_j = l_{\min} + jh, \quad \tau_n = nk, \quad i,j = 0,\ldots,N,$$

$$n = 0,1,2,\ldots .$$

Let be $\phi_{i,j}^n$ the numerical approximation of $\phi(x_i,y_j,\tau_n)$ and $\tilde{\phi}_{i,j}^n$ the non-normalized $\phi_{i,j}^n$. With this notation, the normalized CN scheme in two dimensions reads

$$\frac{\tilde{\phi}_{i,j}^n - \phi_{ij}^n}{k} = \frac{1}{4\tilde{m}h^2}(\tilde{\phi}_{i+1,j}^{n+1} - 2\tilde{\phi}_{i,j}^{n+1} + \tilde{\phi}_{i-1,j}^{n+1} + \phi_{i+1,j}^n - 2\phi_{i,j}^n + \phi_{i-1,j}^n) + \frac{1}{4\tilde{m}h^2}(\tilde{\phi}_{i,j+1}^{n+1} - 2\tilde{\phi}_{i,j}^{n+1} + \tilde{\phi}_{i,j-1}^{n+1} + \phi_{i,j+1}^n - 2\phi_{i,j}^n + \phi_{i,j-1}^n) - \frac{V_{\mathrm{ext}}(x_i,y_j)}{2}(\tilde{\phi}_{i,j}^{n+1} + \phi_{i,j}^n) - \frac{V_{nl}}{2}|\phi_{i,j}^n|^2(\tilde{\phi}_{i,j}^{n+1} + \phi_{i,j}^n),$$

while the BEFD scheme is given by

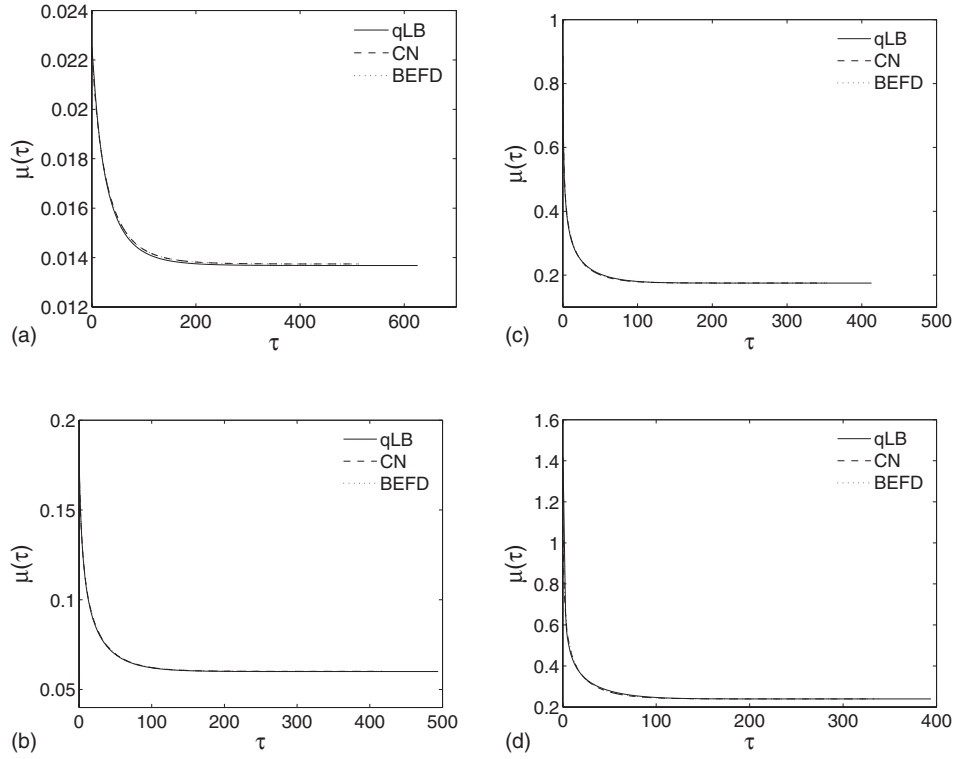

FIG. 2. Chemical potential decay for different values of V_{nl}. Simulation parameters are set as $\tilde{m}=1/8$, $\Delta_0=16$, $\omega_x=1/128$, $nx=1024$. (a) $V_{nl}=1$, (b) $V_{nl}=10$, (c) $V_{nl}=50$, (d) $V_{nl}=80$. Solid lines: qLB model; dashed lines: CN model; dotted lines: BEFD model. Time and chemical potential are expressed in lattice units.

$$\frac{\tilde{\phi}_{i,j}^{n}-\phi_{ij}^{n}}{k}=\frac{1}{2\tilde{m}h^2}(\tilde{\phi}_{i+1,j}^{n+1}-2\tilde{\phi}_{i,j}^{n+1}+\tilde{\phi}_{i-1,j}^{n+1})+\frac{1}{2\tilde{m}h^2}(\tilde{\phi}_{i,j+1}^{n+1}-2\tilde{\phi}_{i,j}^{n+1}+\tilde{\phi}_{i,j-1}^{n+1})-V_{\mathrm{ext}}(x_i,y_j)\tilde{\phi}_{i,j}^{n+1}-V_{nl}|\phi_{i,j}^{n}|^2\tilde{\phi}_{i,j}^{n+1}$$

for $i,j=1,\ldots,N-1$ and $n=0,1,2,\ldots$. Dirichlet boundary conditions are imposed for both schemes

$$\tilde{\phi}_{0,j}^{n+1}=\tilde{\phi}_{i,0}^{n+1}=\tilde{\phi}_{N,j}^{n+1}=\tilde{\phi}_{i,N}^{n+1}=0,\quad i,j=0,\ldots,N,\quad n=0,1,2,\ldots,$$

and the normalization step is performed as follows:

$$\phi_{i,j}^{n+1}=\frac{\tilde{\phi}_{i,j}^{n+1}}{\|\tilde{\phi}^{n+1}\|},$$

for $i,j=0,\ldots,N$ and $n=0,1,2,\ldots$.

VIII. THOMAS-FERMI APPROXIMATION

It is useful to discuss the solution of the Gross-Pitaevskii equation in the so-called Thomas-Fermi approximation, which corresponds to the strong-interaction limit in which kinetic energy contributions can be neglected [21]. This limit is reached by setting large values of the parameter NU_d.

Consider the time-independent GPE of Eq. (8), by ignoring the kinetic energy term, we have

$$\hbar\mu_{\mathrm{TF}}\phi(\boldsymbol{r})=[V_{\mathrm{ext}}(\boldsymbol{r})+NU_d|\phi(\boldsymbol{r})|^2]\phi(\boldsymbol{r}),$$

where we indicate μ with μ_{TF} to recall that this is the Thomas-Fermi chemical potential. In this case, the solution of the GPE is trivial and the wave function $\phi(\boldsymbol{r})$ satisfies

$$|\phi(\boldsymbol{r})|^2=\begin{cases}\dfrac{\hbar}{NU_d}\left(\mu_{\mathrm{TF}}-\dfrac{V_{\mathrm{ext}}(\boldsymbol{r})}{\hbar}\right) & \text{if } \mu>\dfrac{V_{\mathrm{ext}}(\boldsymbol{r})}{\hbar},\\ 0 & \text{otherwise.}\end{cases}\quad (50)$$

The chemical potential given by this approximation μ_{TF} can be found by imposing the normalization condition of Eq. (9).

A. Thomas-Fermi chemical potential in one dimension

We recall that, in one dimension, the harmonic external potential is given by

$$V_{\mathrm{ext}}(x)=\frac{1}{2}m\omega_x^2(x-x_0)^2. \quad (51)$$

The normalization condition of Eq. (9) for the Thomas-Fermi wave function of Eq. (50) is

$$\int_{\mu_{\mathrm{TF}}-V_{\mathrm{ext}}(x)/\hbar>0}\left(\mu_{\mathrm{TF}}-\frac{V_{\mathrm{ext}}(x)}{\hbar}\right)dx=\frac{NU_d}{\hbar}.$$

Including the definition of $V_{\mathrm{ext}}(x)$ of Eq. (51), the condition $\mu_{\mathrm{TF}}-V_{\mathrm{ext}}(x)/\hbar>0$ implies

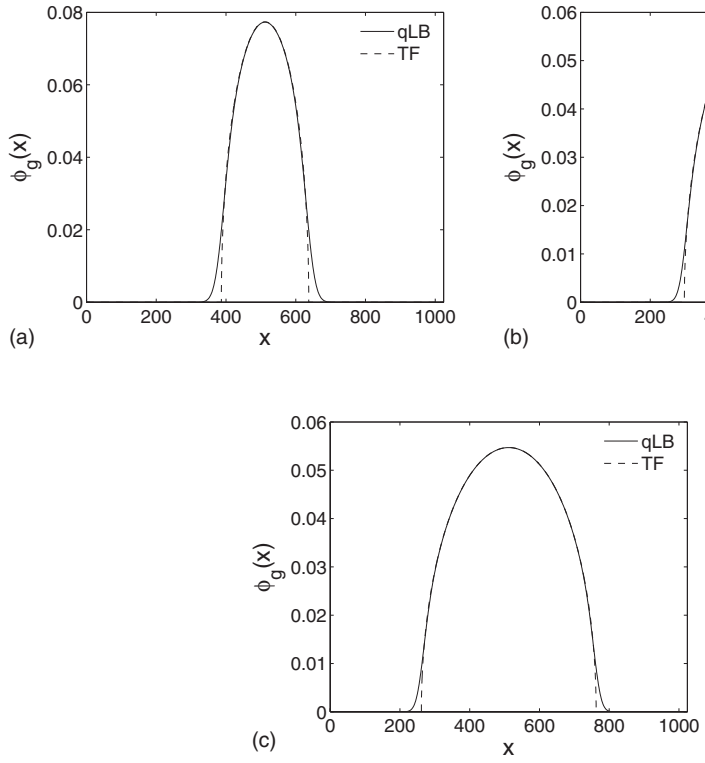

FIG. 3. Ground-state profile $\phi_g(x)$ for different values of V_{nl}. Simulation parameters are set as $\tilde{m}=1/8$, $\Delta_0=16$, $\omega_x=1/128$, $nx=1024$. (a) $V_{nl}=10$, (b) $V_{nl}=50$, (c) $V_{nl}=80$. Solid lines: qLB model; dashed lines: Thomas-Fermi approximation. Space is expressed in lattice units. The tails associated with the kinetic energy contribution are well visible.

$$x = x_0 \pm \left(\frac{2\mu\hbar}{m\omega_x^2}\right) \equiv x_0 \pm C.$$

Hence, the normalization condition can be written as

$$\int_{x_0-C}^{x_0+C} \mu_{\mathrm{TF}} dx - \frac{1}{2}\frac{m\omega_x^2}{\hbar}\int_{x_0-C}^{x_0+C} (x-x_0)^2 dx = \frac{NU_d}{\hbar}.$$

Upon integrating we obtain

$$\mu_{\mathrm{TF}} = \left(\frac{NU_d}{\hbar}\frac{3}{4}\right)^{2/3}\left(\frac{m\omega_x^2}{2\hbar}\right)^{1/3}.$$

Using the qLB scaling (see the Appendix), we get

$$\mu_{\mathrm{TF}} = \left(\frac{3}{4}V_{nl}\right)^{2/3}\left(\frac{\tilde{m}\omega_x^2}{2}\right)^{1/3}, \tag{52}$$

where each quantity is expressed in lattice units.

B. Thomas-Fermi chemical potential in two dimensions

Let us consider a two-dimensional harmonic potential with $\omega_x=\omega_y\equiv\omega$

$$V_{\mathrm{ext}}(x,y) = \frac{1}{2}m\omega^2(x^2+y^2), \tag{53}$$

in this case, for the sake of simplicity, we assume $(x_0,y_0)=(0,0)$, a choice which does not affect the computation of μ_{TF}.

In order to impose the normalization condition to the Thomas-Fermi wave function of Eq. (50), we need to solve

$$\frac{1}{2}\frac{m\omega^2}{\hbar}(x^2+y^2) < \mu_{\mathrm{TF}}.$$

In polar coordinates $[\rho=(x^2+y^2)^{1/2}, \theta=\arctan(y/x)]$ we have

$$\frac{1}{2}\frac{m\omega^2}{\hbar}\rho^2 < \mu_{\mathrm{TF}},$$

from which

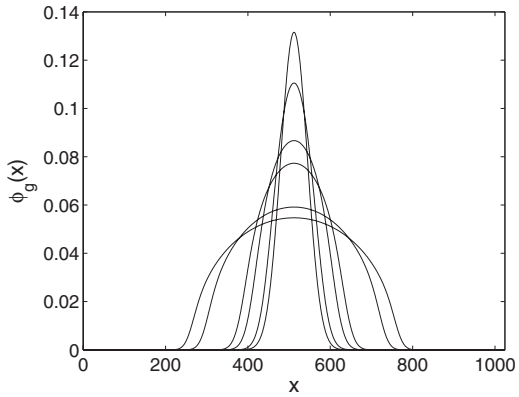

FIG. 4. Ground-state profiles given by the qLB model for different values of V_{nl}. Simulation parameters are set as $\tilde{m}=1/8$, $\Delta_0=16$, $\omega_z=1/128$, $nx=1024$. For increasing values of V_{nl}, curves goes from the top toward the bottom. V_{nl} takes the following values: 0, 1, 5, 10, 50, and 80. Space is expressed in lattice units.

TABLE III. Ground-state chemical potential μ for qLB, CN, and BEFD models. Numerical results are also compared with the Thomas-Fermi chemical potential [see Eq. (54)]. The results are computed for different values of V_{nl}, the other parameters are set as $\omega_x=\omega_y=1/128$, $\tilde{m}=1/8$, $\Delta_{0x}=\Delta_{0y}=16$, $nx=ny=512$.

V_{nl}	μ qLB	μ CN	μ BEFD	μ TF
0	0.007816	0.007812	0.007812	
10	0.009219	0.009250	0.009250	0.004928
100	0.017489	0.017597	0.017597	0.015584
500	0.035802	0.035949	0.035949	0.034846
1000	0.049964	0.050125	0.050125	0.049280
2000	0.070161	0.070338	0.070338	0.069692
3000	0.085721	0.085905	0.085905	0.085355
4000	0.098860	0.099050	0.099050	0.098560
5000	0.110447	0.110642	0.110642	0.110193
10000	0.155967	0.156176	0.156176	0.155837

$$0 < \rho < \left(\frac{2\mu_{\mathrm{TF}}\hbar}{m\omega^2}\right)^{1/2} \equiv C.$$

The normalization condition is then given by

$$\int_0^C \left(\mu_{\mathrm{TF}} - \frac{V_{\mathrm{ext}}(\rho)}{\hbar}\right)\rho d\rho = \frac{NU_d}{2\pi\hbar}.$$

Integrating we obtain

$$\mu_{\mathrm{TF}} = \left(\frac{NU_d}{\hbar^2}\frac{m\omega^2}{\pi}\right)^{1/2}.$$

Using the qLB scaling (see Appendix), we get

$$\mu_{\mathrm{TF}} = \left(\frac{V_{nl}\tilde{m}\omega^2}{\pi}\right)^{1/2}, \tag{54}$$

where each quantity is expressed in lattice units.

IX. NUMERICAL RESULTS

In this section we compare the qLB model against the numerical results obtained by the normalized CN and BEFD schemes, as well as via the Thomas-Fermi approximation.

A. Numerical results in one dimension

Recall that in one dimension and using the qLB scaling [see Eq. (13) and Appendix for details], the potential is given by

$$V(x,\tau) = V_{\mathrm{ext}}(x) + V_{nl}|\phi(x,\tau)|^2$$
$$= \frac{1}{2}\tilde{m}\omega_x^2(x-x_0)^2 + V_{nl}|\phi(x,\tau)|^2.$$

As initial condition, we take a Gaussian packet centered in x_0 and with initial spreading Δ_0

TABLE IV. Maximum value reached by the ground-state wave function $\phi_g(x_0,y_0)$ for qLB, CN, and BEFD models. The results are computed for different values of V_{nl}, the other parameters are set as $\omega_x=\omega_y=1/128$, $\tilde{m}=1/8$, $\Delta_{0x}=\Delta_{0y}=16$, $nx=ny=512$.

V_{nl}	$\phi_g(z_0,y_0)$ qLB	$\phi_g(z_0,y_0)$ CN	$\phi_g(z_0,y_0)$ BEFD
0	0.01723	0.01763	0.01763
10	0.01627	0.01656	0.01656
100	0.01218	0.01226	0.01225
500	0.00835	0.00837	0.00836
1000	0.00702	0.00704	0.00703
2000	0.00590	0.00591	0.00591
3000	0.00533	0.00534	0.00534
4000	0.00496	0.00497	0.00496
5000	0.00469	0.00470	0.00470
10 000	0.00395	0.00395	0.00395

$$\phi(x,0) = (2\pi\Delta_0^2)^{-1/4}\exp\left(-\frac{(x-x_0)^2}{4\Delta_0^2}\right).$$

By working in lattice units (for qLB, CN, and BEFD schemes), we fix a computational domain given by the interval $[0,nx]=[0,1024]$ and set $x_0=512$. Moreover, we set $\Delta_0=16$, $\omega_x=1/128$ and $\tilde{m}=1/8$. For the qLB the discretization steps are fixed at 1 and Dirichlet boundary conditions are used (i.e., $\phi^-=0$ on the boundary). For CN and BEFD schemes, instead, we set $h=0.1$ and $k=0.1$. The models asymptotically tend to a stationary solution. Hence, for all models, the simulation is stopped whenever

$$\max_{i=0,\ldots,N}|\phi_i^{n+1} - \phi_i^n| < \varepsilon,$$

where N is the number of nodal points (and it is smaller for qLB than CN and BEFD) and $\varepsilon=10^{-8}$.

Our results are compared at varying the parameter V_{nl}. In Table I the limit value of μ is reported for qLB, CN, and BEFD models. Moreover, the Thomas-Fermi chemical potential μ_{TF} given by Eq. (52) is also shown. We observe that, for $V_{nl}\geqslant 40$, the qLB chemical potential becomes slightly smaller than the Thomas-Fermi chemical potential, which should always be a lower bound instead. However, by increasing the accuracy of the qLB model (i.e., halving the discretization step) the values of μ_{qLB} becomes larger than μ_{TF} (see Sec. X for details), as they should. In Table II, the maximum value of ϕ at the end of the simulation $[\phi_g(x_0)]$ is reported for all the three models.

In Fig. 1, we compare the ground-state wave function $\phi_g(x)$ given by the models for some values of V_{nl}, in Fig. 2 the same comparison is reported for the chemical potential decay profiles. In Fig. 3, we compare the ground state profile given by the qLB model with the wave function of the Thomas-Fermi approximation of Eq. (50) for some values of V_{nl}. Finally, in Fig. 4, we report the ground-state profiles given by qLB varying V_{nl}.

B. Numerical results in two dimensions

In this section we present results referring to the following two-dimensional potential:

$$V(x,y,\tau) = V_{\text{ext}}(x,y) + V_{nl}|\phi(x,y,\tau)|^2 = \frac{1}{2}\tilde{m}[\omega_x^2(x-x_0)^2 + \omega_y^2(y-y_0)^2] + V_{nl}|\phi(x,y,\tau)|^2.$$

As initial condition, we consider a Gaussian packet centered in (x_0,y_0) and with initial spreads Δ_{0x}, Δ_{0y} along x and y, respectively,

$$\phi(x,y,0) = (2\pi\Delta_{0x}\Delta_{0y})^{-1/2} \times \exp\left(-\frac{(x-x_0)^2}{4\Delta_{0x}^2}\right)\exp\left(-\frac{(y-y_0)^2}{4\Delta_{0y}^2}\right). \quad (55)$$

Let $[0,nx]\times[0,ny]=[0,512]\times[0,512]$ be our domain and $(x_0,y_0)=(256,256)$, furthermore we fix $\Delta_{0x}=\Delta_{0y}=16$, $\omega_x=\omega_y=1/128$, and $\tilde{m}=1/8$. Discretization steps for the qLB model are again fixed to unity, while for CN and BEFD we set $h=0.5$ and $k=0.1$. Dirichlet boundary conditions are imposed in all qLB simulations. The stop condition for the simulation is

$$\max_{i,j=0,\ldots,N} |\phi_{i,j}^{n+1} - \phi_{i,j}^{n}| < \varepsilon,$$

with $\varepsilon=10^{-9}$.

In Table III the limit value of μ is reported for the three models. Moreover, the Thomas-Fermi chemical potential μ_{TF} given by Eq. (54) is also shown. In Table IV, the maximum value of ϕ at the end of the simulation $[\phi_g(x_0,y_0)]$ computed by qLB, CN, and BEFD is reported.

In Fig. 5, we compare the ground-state wave function $\phi_g(x,y)$ taken at $y=y_0$ given by the models for some values of V_{nl}, in Fig. 6 the same comparison is reported for the chemical potential decay profiles. In Fig. 7, we compare the ground state profile taken at $y=y_0$ given by the qLB model with the wave function of the Thomas-Fermi approximation of Eq. (50) for some values of V_{nl}. Finally, in Fig. 8, we report the ground-state profiles given by qLB varying V_{nl} at the cross section $y=y_0$.

These data witness a satisfactory agreement between qLB and the reference CN and BEFD solutions, while CN and BEFD are in excellent agreement with each other (this is due to the high resolution adopted in these reference cases).

As a second example, we consider an external potential where a Gaussian stirring term (representing, for example, a far-blue detuned laser beam [22]) is added to the harmonic trap

$$V_{\text{ext}}(x,y) = \frac{1}{2}\tilde{m}[\omega_x^2(x-x_0)^2 + \omega_y^2(y-y_0)^2] + \omega_0 e^{-\delta\{[(x-x_0)-r_0]^2+(y-y_0)^2\}}. \quad (56)$$

A similar example is given in Ref. [14]. As mentioned in Ref. [14], in the time-dependent GPE, such a potential [where the stirring Gaussian term is itself time-dependent through the motion of the center $r_0(t)$] is used to generate vortices in BEC [22,23]. The initial condition is still given by the Gaussian packet given in Eq. (55). We consider the computational domain $[0,nx]\times[0,ny]=[0,512]\times[0,512]$ and $x_0=y_0=256$ and we choose $\tilde{m}=1/8$, $\Delta_{0x}=\Delta_{0y}=22.63$, $\omega_x=\omega_y=1/128$, $V_{nl}=1000$, $\omega_0=8/128$, $r_0=50$, and $\delta=1/512$. For CN and BEFD schemes, we set $h=0.5$ and $k=0.1$, while for the qLB scheme the discretization steps are set to unit value. With these parameters, the ground-state chemical potentials computed by qLB, CN, and BEFD schemes are as follows:

$$\mu_{\text{qLB}} = 0.052238, \quad \mu_{\text{CN}} = 0.052408, \quad \mu_{\text{BEFD}} = 0.052408.$$

In Fig. 9 a comparison between the chemical potential decays obtained by qLB, CN, and BEFD models is reported. Finally, in Fig. 10, the ground state surfaces computed by qLB, CN, and BEFD models are shown by plotting the isolines taken at different values of $|\phi_g(x,y)|$. Again, a satisfactory agreement between qLB and the reference CN and BEFD results is generally observed.

X. HALVING THE DISCRETIZATION STEP

One of the distinctive properties of qLB, as opposed to usual explicit schemes for quantum wave equations, is that the time-step scales linearly with the mesh spacing. In order to verify this linear dependence, we halved Δx (and consequently $\Delta\tau$) while keeping ω_c fixed and we checked the model still gives the same solution.

As an example, we consider the interval [0,1024] and set $\tilde{m}=1/8$, $\omega_x=1/128$, $\Delta_0=16$, and $V_{nl}=10$. To make a comparison, we compute the solution with CN and BEFD schemes for $h=0.0625$ and $k=0.1$. In Table V the values of μ obtained halving Δ are reported. The "exact" value given by CN and BEFD models with a very small spatial discretization step is $\mu_{\text{exact}}=0.060112$. We can observe that, by halving Δ, the value of μ given by the qLB model increases towards μ_{exact}. In Fig. 11 $\phi_g(x)$ is plotted for different values of Δ and the curves are almost coinciding.

Although a systematic study of the computational efficiency of the qLB method lies beyond the scope of the present work, as an indication, we just provide some representative data on the computational performance of the scheme. To this end, we consider a domain $[0,256]\times[0,256]$ and set $\tilde{m}=1/8$, $\omega_x=\omega_y=1/128$, $\Delta_{0x}=\Delta_{0y}=16$, and $V_{nl}=50$. The simulation is stopped when time $T_{\max}=1000$ is reached. To compare qLB, CN, and BEFD performances, we choose the same mesh-spacing and time step for the three models

$$\Delta \equiv \Delta x = \Delta y = -i\Delta\tau = h = k,$$

and Δ is initially set to unit value and then halved twice. In Table VI, the CPU times required by the models on a standard PC (Intel Pentium 4 CPU 3 GHz) are reported. These data indicate that qLB performs competitively with respect to CN and BEFD, especially as grid resolution is increased.

XI. CONCLUSIONS AND OUTLOOK

Summarizing, we have extended the multidimensional quantum Lattice Boltzmann method to the case of nonlinear

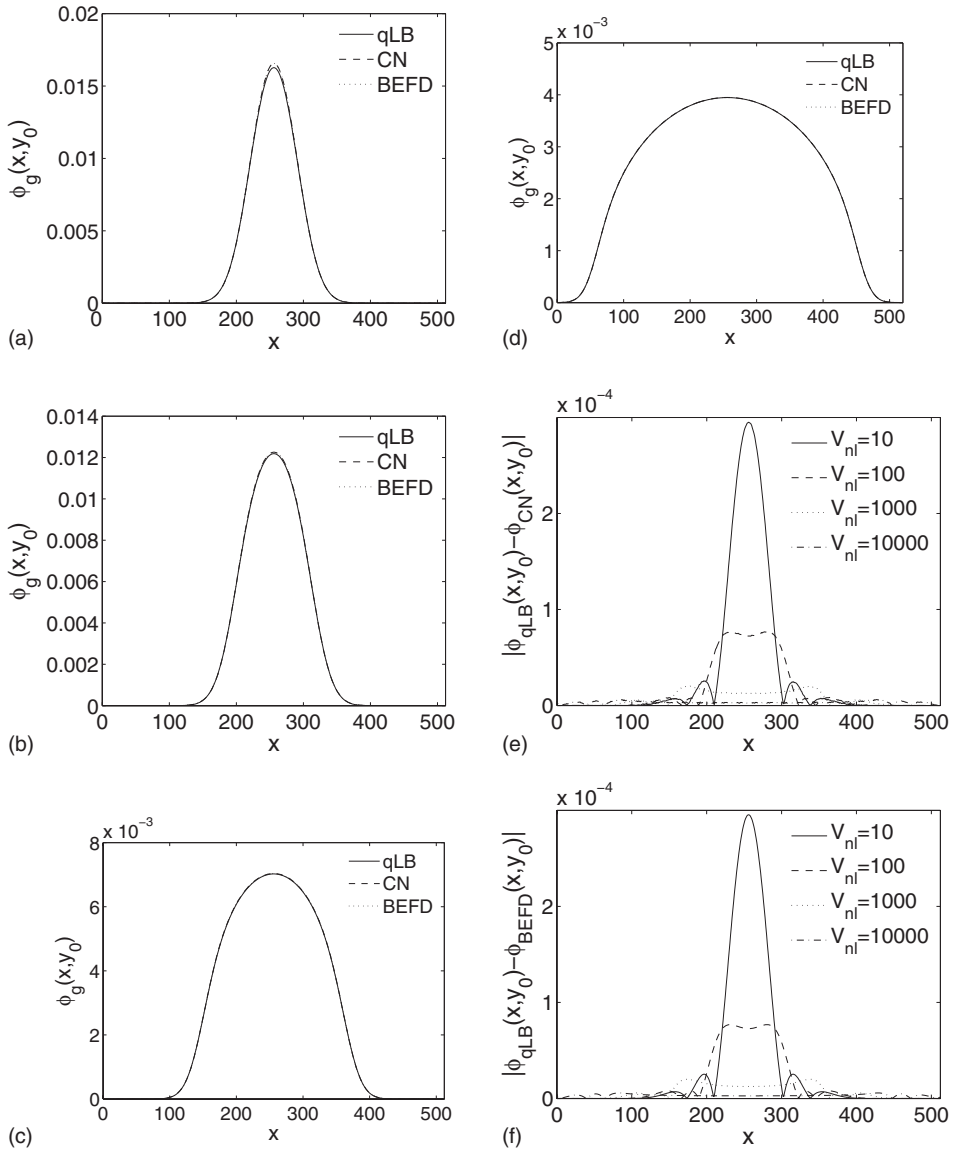

FIG. 5. Ground-state profile $\phi_g(x,y)$ taken at $y=y_0$ for different values of V_{nl}. Simulation parameters are set as $\tilde{m}=1/8$, $\Delta_{0x}=\Delta_{0y}=16$, $\omega_x=\omega_y=1/128$, $nx=ny=512$. (a) $V_{nl}=10$, (b) $V_{nl}=100$, (c) $V_{nl}=1000$, (d) $V_{nl}=10\,000$. Solid lines: qLB model; dashed lines: CN model; dotted lines: BEFD model. The deviations of qLB from CN and BEFD are not visible on this scale, hence in (e) and (f) the differences $|(\phi_g)_{\mathrm{qLB}}(x,y_0)-(\phi_g)_{\mathrm{CN}}(x,y_0)|$ and $|(\phi_g)_{\mathrm{qLB}}(x,y_0)-(\phi_g)_{\mathrm{BEFD}}(x,y_0)|$ computed at the qLB nodal points are plotted. Space is expressed in lattice units.

quantum wave equations, most notably the Gross-Pitaevskii equation describing the dynamics of zero-temperature Bose-Einstein condensates. The nonlinear qLB is applied to the numerical computation of the ground state of the GPE in one and two dimensions, and its viability demonstrated through systematic comparison with numerical solutions obtained via standard implicit methods, as well as with analytical results based on the Thomas-Fermi approximation. Being based on a first-order, relativistic formulation, at variance with most explicit schemes for nonrelativistic quantum wave equations, the QLB method offers stable operation with a time-step scaling only linearly with the size of spatial mesh spacing. Although a systematic comparison of efficiency/accuracy with existing methods for nonlinear quantum wave equations is beyond the scope of the present work, the qLB appears to provide a satisfactory computational performance, the computation of a two-dimensional ground state on a 512×512 requiring just a few minutes CPU time on a standard PC. Future extension of the present qLB scheme to the case of nonlocal interactions, as well as to quantum flows in confined geometries are currently underway.

APPENDIX: FROM QLB TO PHYSICAL UNITS

Let us consider the Gross-Pitaevskii equation in three dimensions expressed in physical units

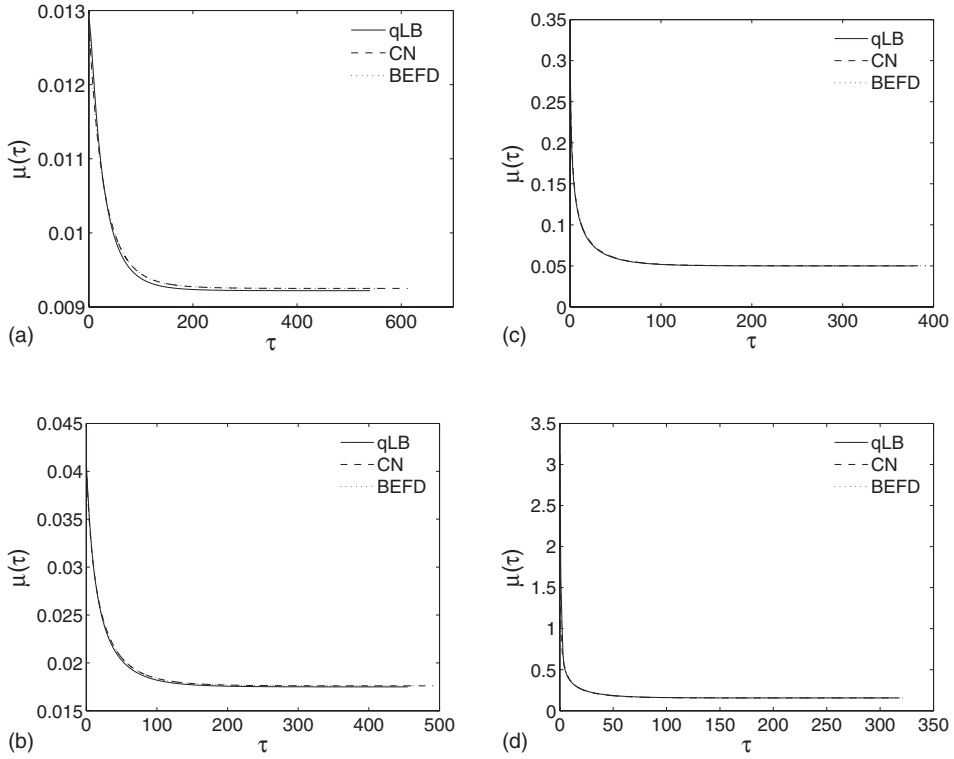

FIG. 6. Chemical potential decay for different values of V_{nl}. Simulation parameters are set as $\tilde{m}=1/8$, $\Delta_{0x}=\Delta_{0y}=16$, $\omega_x=\omega_y=1/128$, $nx=ny=512$. (a) $V_{nl}=10$, (b) $V_{nl}=100$, (c) $V_{nl}=1000$, (d) $V_{nl}=10\,000$. Solid lines: qLB model; dashed lines: CN model; dotted lines: BEFD model. Time and chemical potential are expressed in lattice units.

$$i\hbar\frac{\partial\psi(\boldsymbol{r},t)}{\partial t}=\left(-\frac{\hbar^2}{2m}\Delta_{\boldsymbol{r}}+V_{\text{ext}}(\boldsymbol{r})+NU_0|\psi(\boldsymbol{r},t)|^2\right)\psi(\boldsymbol{r},t), \tag{A1}$$

where $\boldsymbol{r}=(x,y,z)^T$ and $V_{\text{ext}}(\boldsymbol{r})=(1/2)m\omega_H^2\boldsymbol{r}^2$ and we are assuming, for the sake of simplicity, $\omega_x=\omega_y=\omega_z\equiv\omega_H$ and we recall that $U_0=4\pi\hbar^2a/m$. The qLB scaling is given by

$$\tilde{t}=t/\Delta t,\quad \tilde{\boldsymbol{r}}=\boldsymbol{r}/\Delta r,\quad \text{where } (\Delta x=\Delta y=\Delta z\equiv\Delta r),$$

$$\tilde{\psi}(\tilde{\boldsymbol{r}},\tilde{t})=(\Delta r)^{3/2}\psi(\boldsymbol{r},t),\quad \tilde{\omega}_H=\omega_H\Delta t. \tag{A2}$$

Furthermore, we define the harmonic unit l_H:

$$l_H^2=\frac{\hbar}{m\omega_H}. \tag{A3}$$

Applying the qLB scaling of Eq. (A2) to Eq. (A1), we obtain

$$i\partial_{\tilde{t}}\tilde{\psi}=-\frac{\hbar}{2m}\frac{\Delta t}{(\Delta r)^2}\Delta_{\tilde{r}}\tilde{\psi}+\frac{1}{2}\frac{m\tilde{\omega}_H^2}{\hbar}\frac{(\Delta r)^2}{\Delta t}\tilde{\boldsymbol{r}}^2+\frac{NU_0}{\hbar}\frac{\Delta t}{(\Delta r)^3}|\tilde{\psi}|^2\tilde{\psi}.$$

Let us indicate each term as follows:

$$\tilde{D}=-\frac{\hbar}{2m}\frac{\Delta t}{(\Delta r)^2}, \tag{A4}$$

$$\tilde{V}_{\text{ext}}=\frac{1}{2}\frac{m\tilde{\omega}_H^2}{\hbar}\frac{(\Delta r)^2}{\Delta t}\tilde{\boldsymbol{r}}^2, \tag{A5}$$

$$\tilde{V}_{nl}=\frac{NU_0}{\hbar}\frac{\Delta t}{(\Delta r)^3}. \tag{A6}$$

Moreover, recall that the qLB is numerically solving the following equations:

$$\partial_t\psi\pm c\partial_x\psi=\pm\omega_c\psi,$$

with

$$\omega_c=\frac{mc^2}{\hbar}. \tag{A7}$$

Scaling these equations, we obtain

$$\partial_{\tilde{t}}\tilde{\psi}\pm c\frac{\Delta t}{\Delta r}\partial_{\tilde{x}}\tilde{\psi}=\pm(\omega_c\Delta t)\tilde{\psi},$$

so that the following relations must be imposed:

$$c\frac{\Delta t}{\Delta r}=1, \tag{A8}$$

$$\omega_c\Delta t=\tilde{m}. \tag{A9}$$

From relation of Eq. (A8) it is apparent that in order to simulate physical situations we must take c much smaller than the physical light speed. Otherwise, we would need a very small time step to achieve a reasonable Δr. In particular, we make the following position:

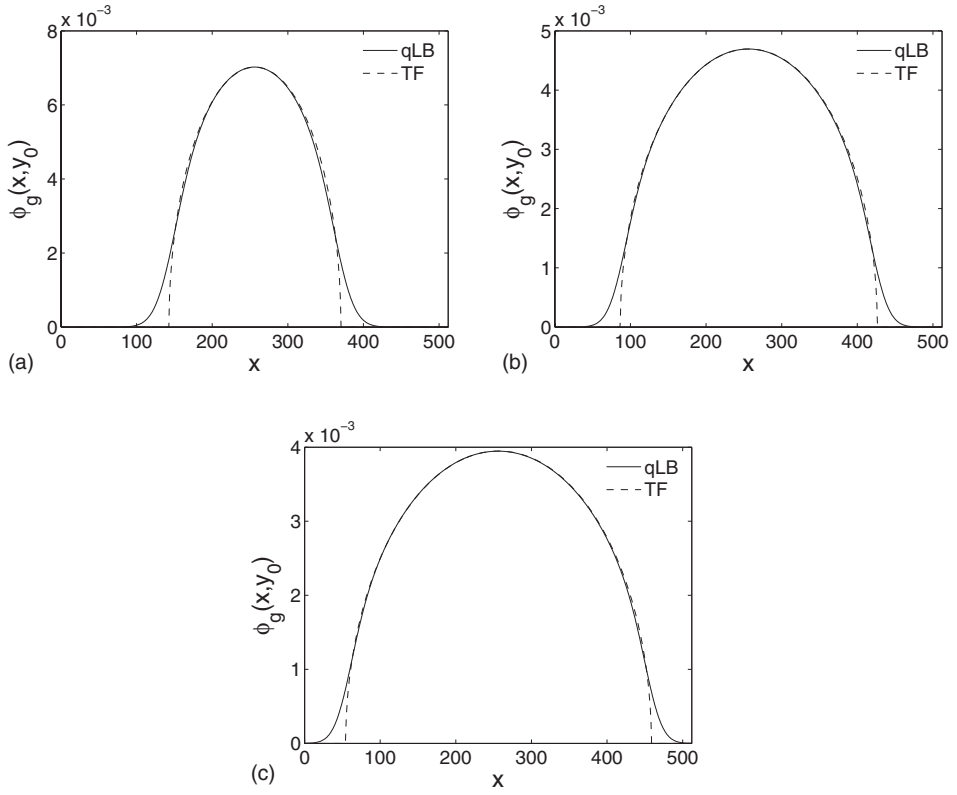

FIG. 7. Ground-state profile $\phi_g(x,y)$ taken at $y=y_0$ for different values of V_{nl}. Simulation parameters are set as $\tilde{m}=1/8$, $\Delta_{0x}=\Delta_{0y}=16$, $\omega_x=\omega_y=1/128$, $nx=ny=512$. (a) $V_{nl}=1000$, (b) $V_{nl}=5000$, (c) $V_{nl}=10\,000$. Solid lines: qLB model; dashed lines: Thomas-Fermi approximation. Space is expressed in lattice units. The tails associated with the kinetic energy contribution are well visible.

$$c = l_H \omega_H. \tag{A10}$$

From this position and the definition of ω_c given in Eq. (A7), we obtain

$$\frac{\omega_H \hbar}{m} = l_H^2 \omega_H^2 = c^2 = \frac{\omega_c \hbar}{m}$$

and then

$$\omega_H = \omega_c.$$

Hence, from Eq. (A9), we have

$$\omega_H \Delta t = \tilde{m}. \tag{A11}$$

From position of Eq. (A10) and Eqs. (A8) and (A11) we have

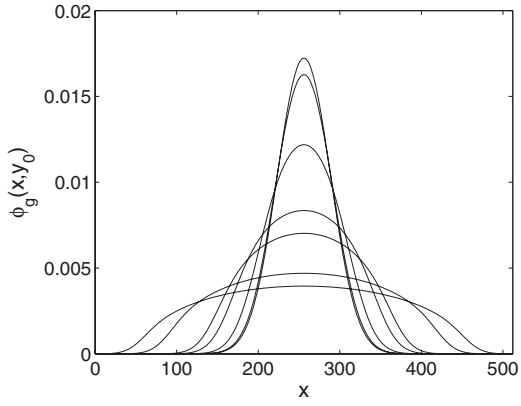

FIG. 8. Ground-state profiles given by the qLB model for different values of V_{nl}. Simulation parameters are set as $\tilde{m}=1/8$, $\Delta_{0x}=\Delta_{0y}=16$, $\omega_x=\omega_y=1/128$, $nx=ny=512$. For increasing values of V_{nl}, curves go from the top to bottom. V_{nl} takes the following values: 0, 10, 100, 500, 1000, 5000, and 10 000. Space is expressed in lattice units.

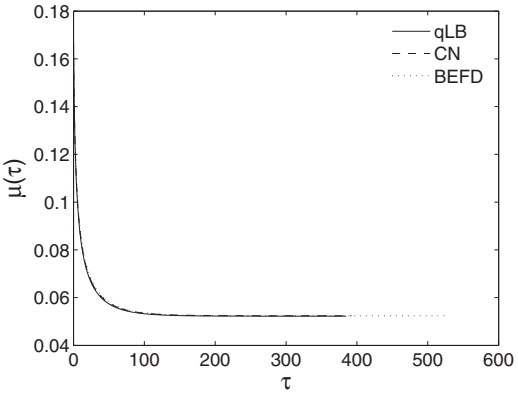

FIG. 9. Chemical potential decay profiles given by qLB, CN, and BEFD models with the external potential of Eq. (56). Simulation parameters are set as $\tilde{m}=1/8$, $\Delta_{0x}=\Delta_{0y}=22.63$, $\omega_x=\omega_y=1/128$, $nx=ny=512$, $V_{nl}=1000$, $\omega_0=8/128$, $r_0=50$, and $\delta=1/512$. Solid line: qLB; dashed line: CN; dotted line: BEFD. Time and chemical potential are expressed in lattice units.

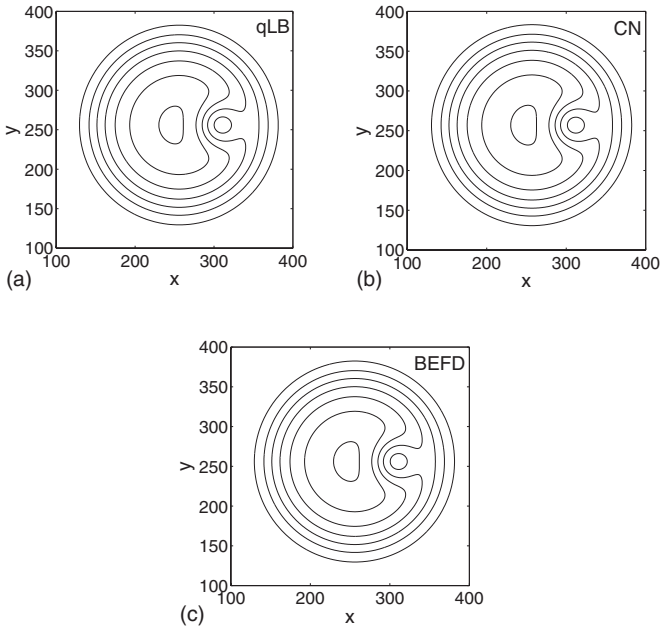

FIG. 10. Ground-state contour plots computed by qLB, CN, and BEFD models with the external potential of Eq. (56). Simulation parameters are set as $\tilde{m}=1/8$, $\Delta_{0x}=\Delta_{0y}=22.63$, $\omega_x=\omega_y=1/128$, $nx=ny=512$, $V_{nl}=1000$, $\omega_0=8/128$, $r_0=50$, and $\delta=1/512$. (a) qLB model, (b) CN model, (c) BEFD model. The isolines correspond to the following values of $\phi_g(x,y)$: 0.001, 0.002, 0.003, 0.004, 0.005, 0.006, and 0.007 going from the outside toward the inside. Space is expressed in lattice units.

$$\frac{l_H\omega_H\Delta t}{\Delta r}=\frac{l_H\tilde{m}}{\Delta r}=1$$

and then

$$\frac{l_H}{\Delta r}=\frac{1}{\tilde{m}}. \tag{A12}$$

Consider now $\tilde{D}$ [see Eq. (A4)], multiplying and dividing it by ω_H and l_H^2, we obtain

TABLE V. Chemical potential μ obtained halving the discretization step Δ. Simulation parameters are set as $\tilde{m}=1/8$, $\omega_x=1/128$, $\Delta_0=16$, and $V_{nl}=10$.

Δ	μ
1	0.060010
0.5	0.060026
0.25	0.060040
0.125	0.060059
0.0625	0.060096
μ_{exact}	0.060112

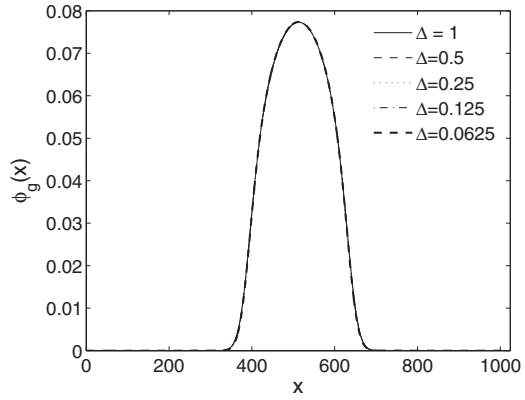

FIG. 11. Ground-state profiles for different values of Δ. Simulation parameters are set as $\tilde{m}=1/8$, $\omega_x=1/128$, $\Delta_0=16$, and $V_{nl}=10$. Space is expressed in lattice units.

$$\tilde{D}=\frac{\hbar\Delta t}{2m(\Delta r)^2}=(\omega_H\Delta t)\left(\frac{l_H}{\Delta r}\right)^2\frac{\hbar}{2m}\frac{1}{\omega_H l_H^2}$$
$$=\frac{1}{2}(\omega_H\Delta t)\left(\frac{l_H}{\Delta r}\right)^2=\frac{1}{2\tilde{m}}, \tag{A13}$$

where we used relations of Eqs. (A11) and (A12) in the last equality.

As for $\tilde{V}_{\text{ext}}$, we have

$$\tilde{V}_{\text{ext}}=\frac{1}{2}\frac{m\tilde{\omega}_H^2}{\hbar}\frac{(\Delta r)^2}{\Delta t}\frac{\omega_H}{\omega_H}=\frac{1}{2}\left(\frac{\Delta r}{l_H}\right)^2\frac{\tilde{\omega}_H^2}{\Delta t\omega_H}=\frac{1}{2}\tilde{m}\tilde{\omega}_H^2, \tag{A14}$$

where we used relations (A11) and (A12) in the last equality. Finally, consider $\tilde{V}_{nl}$. Multiplying and dividing by l_H^2, we have

$$\tilde{V}_{nl}=N\frac{4\pi\hbar a}{m}\frac{\Delta t}{(\Delta r)^3}l_H^2\frac{m\omega_H}{\hbar}=4\pi N(\omega_H\Delta t)\frac{al_H^2}{(\Delta r)^3}.$$

Multiplying and dividing again by l_H, we obtain

$$\tilde{V}_{nl}=N4\pi(\omega_H\Delta t)\frac{a}{l_H}\left(\frac{l_H}{\Delta r}\right)^3=N4\pi\frac{a}{l_H}\frac{1}{\tilde{m}^2}, \tag{A15}$$

where we used Eqs. (A11) and (A12). For a typical set of physical parameters we have $a/l_H\approx 10^{-4}$ and usually we set

TABLE VI. CPU times required by qLB, CN, and BEFD models using the same mesh spacing and time step. The discretization step Δ is initially set to unit value and then halved twice. Simulation parameters are as follows: $\tilde{m}=1/8$, $\omega_x=\omega_y=1/128$, $\Delta_{0x}=\Delta_{0y}=16$, $V_{nl}=50$, and $T_{\max}=1000$.

Δ	Mesh size	CPU time qLB (s)	CPU time CN (s)	CPU time BEFD (s)
1	256×256	95	81	114
0.5	512×512	760	810	1014
0.25	1024×1024	6120	9544	10672

$\tilde{m} \approx 10^{-1}$, hence, given the value of $\tilde{V}_{nl}$ in lattice units, the number of physical particles composing the condensate is approximately

$$N = \frac{\tilde{V}_{nl}}{4\pi} 10^2.$$

From Eqs. (A13)–(A15), removing all the $\tilde{\cdot}$ (apart from $\tilde{m}$, in order to not confuse this scaling parameter with the particle mass), we conclude that, with the qLB scaling, the GPE given in Eq. (A1) becomes

$$i\frac{\partial \psi(\boldsymbol{r},t)}{\partial t} = \left(-\frac{1}{2\tilde{m}}\Delta_{\boldsymbol{r}} + \frac{1}{2}\tilde{m}\omega_H^2 \boldsymbol{r}^2 + V_{nl}|\psi(\boldsymbol{r},t)|^2 \right) \psi(\boldsymbol{r},t),$$

where each quantity is expressed in lattice units.

[1] F. Dalfovo, S. Giorgini, L. P. Pitaevskii, and S. Stringari, Rev. Mod. Phys. **71**, 463 (1999).
[2] A. J. Legget, Rev. Mod. Phys. **73**, 307 (2001).
[3] E. P. Gross, Nuovo Cimento **20**, 454 (1961).
[4] L. P. Pitaevskii, Sov. Phys. JETP **13**, 451 (1961).
[5] G. R. McNamara and G. Zanetti, Phys. Rev. Lett. **61**, 2332 (1988).
[6] R. Benzi, S. Succi, and M. Vergassola, Phys. Rep. **222**, 145 (1992).
[7] S. Succi and R. Benzi, Physica D **69**, 327 (1993).
[8] S. Succi, Phys. Rev. E **53**, 1969 (1996).
[9] S. Palpacelli and S. Succi, Phys. Rev. E **75**, 066704 (2007).
[10] A. D. Jackson, G. M. Kavoulakis, and C. J. Pethick, Phys. Rev. A **58**, 2417 (1998).
[11] P. Leboeuf and N. Pavloff, Phys. Rev. A **64**, 033602 (2001).
[12] W. Bao and W. Tang, J. Comput. Phys. **187**, 230 (2003).
[13] S. K. Adhikari, Phys. Rev. E **62**, 2937 (2000).
[14] W. Bao and Q. Du, SIAM J. Sci. Comput. (USA) **25**, 1674 (2004).
[15] W. Bao, I. Chern, and F. Y. Lim, J. Comput. Phys. **219**, 836 (2006).
[16] A. Aftalion and Q. Du, Phys. Rev. A **64**, 063603 (2001).
[17] M. M. Cerimele, M. L. Chiofalo, F. Pistella, S. Succi, and M. P. Tosi, Phys. Rev. E **62**, 1382 (2000).
[18] M. L. Chiofalo, S. Succi, and M. P. Tosi, Phys. Rev. E **62**, 7438 (2000).
[19] A. Minguzzi, S. Succi, F. Toschi, M. P. Tosi, and P. Vignolo, Phys. Rep. **395**, 223 (2004).
[20] L. Landau and E. Lifshitz, *Relativistic Quantum Field Theory* (Pergamon, Oxford, 1960).
[21] F. Dalfovo, L. Pitaevskii, and S. Stringari, J. Res. Natl. Inst. Stand. Technol. **101**, 537 (1996).
[22] B. M. Caradoc-Davies, R. J. Ballagh, and K. Burnett, Phys. Rev. Lett. **83**, 895 (1999).
[23] B. Jackson, J. F. McCann, and C. S. Adams, Phys. Rev. Lett. **80**, 3903 (1998).